Low-cost hand-held probe for depth-resolved low-coherence interferometry

PARITOSH PANDE,[1] RYAN L. SHELTON,[1] GUILLERMO L. MONROY,[1,2] RYAN M. NOLAN,[1] AND STEPHEN A. BOPPART[1,2,3,4,*]

[1]*Beckman Institute for Advanced Science and Technology, University of Illinois at Urbana-Champaign, Urbana, Illinois, USA*
[2]*Department of Bioengineering, University of Illinois at Urbana-Champaign, Urbana, Illinois, USA*
[3]*Department of Electrical and Computer Engineering, University of Illinois at Urbana-Champaign, Urbana, Illinois, USA*
[4]*Department of Internal Medicine, University of Illinois at Urbana-Champaign, Urbana, Illinois, USA*
[*]*boppart@illinois.edu*

Abstract: We report on the development of a low-cost hand-held low-coherence interferometric imaging system based on the principle of linear optical coherence tomography (Linear OCT), a technique which was first proposed in the early 2000s as a simpler alternative to the conventional time-domain and Fourier-domain OCT. A bench-top implementation of the proposed technique is first presented and validated. The axial resolution, SNR, and sensitivity roll-of of the system was estimated to be 5.2 μm and 80 dB, and 3.7 dB over a depth of 0.15 mm, respectively. After validating the bench-top system, two hand-held probe implementations for contact-based imaging and *in vivo* human tympanic membrane imaging are presented. The performance of the proposed system was compared with a research-grade state-of-the-art Fourier-domain low coherence interferometry (LCI) system by imaging several biological and non-biological samples. The results of this study suggest that the proposed system might be a suitable choice for applications where imaging depth and SNR can be traded for lower cost and simpler optical design.

© 2016 Optical Society of America

References and links

1. J. A. Izatt and M. A. Choma, "Theory of optical coherence tomography," in *Optical Coherence Tomography*, W. Drexler, J. G. Fujimoto ed. (Springer, 2008).
2. E. A. Swanson, D. Huang, C. P. Lin, C. A. Puliafito, M. R. Hee, and J. G. Fujimoto, "High-speed optical coherence domain reflectometry," Opt. Lett. **17**(2), 151–153 (1992).
3. A. F. Fercher, C. K. Hitzenberger, G. Kamp, and S. Y. El-Zaiat, "Measurement of intraocular distances by backscattering spectral interferometry," Opt. Commun. **117**(1), 43–48 (1995).
4. M. A. Choma, M. V. Sarunic, C. Yang, and J. A. Izatt, "Sensitivity advantage of swept source and Fourier domain optical coherence tomography," Opt. Express **11**(18), 2183–2189 (2003).
5. W. Jung, J. Kim, M. Jeon, E. J. Chaney, C. Stewart, and S. A. Boppart, "Handheld optical coherence tomography scanner for primary care diagnostics," IEEE Trans. Biomed. Eng. **58**(3), 741–744 (2011).
6. C. D. Lu, M. F. Kraus, B. Potsaid, J. J. Liu, W. Choi, V. Jayaraman, A. E. Cable, J. Hornegger, J. S. Duker, and J. G. Fujimoto, "Handheld ultrahigh speed swept source optical coherence tomography instrument using a MEMS scanning mirror," Biomed. Opt. Express **5**(1), 293–311 (2014).
7. Y. Huang, G. J. Furtmüller, D. Tong, S. Zhu, W. P. Andrew Lee, G. Brandacher, J. U Kang, "MEMS-based handheld Fourier domain Doppler optical coherence tomography for intraoperative microvascular anastomosis imaging," PloS One **9**(12), e114215 (2014).
8. A. Cogliati, C. Canavesi, A. Hayes, P. Tankam, V-F. Duma, A. Santhanam, K. P Thompson, and J. P Rolland, "MEMS-based handheld scanning probe with pre-shaped input signals for distortion-free images in Gabor-domain optical coherence microscopy," Opt. Express **24**(12), 3365–13374 (2016).
9. R. Dsouza, H. Subhash, K. Neuhaus, J. Hogan, C. Wilson, and M. Leahy, "Dermascope guided multiple reference optical coherence tomography," Biomed. Opt. Express **5**(9), 2870–2882 (2014).
10. C. Hauger, M. Wörz, and T. Hellmuth, "Interferometer for optical coherence tomography," Appl. Opt. **42**(19), 3896–3902 (2003).
11. P. Koch, G. Hüttmann, H. Schleiermacher, J. Eichholz, and E. Koch, "Linear optical coherence tomography system with a downconverted fringe pattern," Opt. Lett. **29**(14), 1644–1646 (2004).

12. P. Koch, V. Hellemanns, and G. Hüttmann, "Linear optical coherence tomography system with extended measurement range," Opt. Lett. **31**(19), 2882–2884 (2006).

13. M. Takeda, H. Ina, and S. Kobayashi, "Fourier-transform method of fringe-pattern analysis for computer-based topography and interferometry," J. Opt. Soc. Am. **72**(1), 156–160 (1982).

14. P. Pande, R. L. Shelton, G. L. Monroy, R. M. Nolan, and S. A. Boppart, "A mosaicking approach for *in vivo* thickness mapping of the human tympanic membrane using low coherence interferometry," J. Assoc. Res. Otolaryngol. **17**(5), 403–416 (2016).

15. C. T. Nguyen, W. Jung, J. Kim, E. J. Chaney, M. Novak, C. N. Stewart, and S. A. Boppart, "Noninvasive *in vivo* optical detection of biofilm in the human middle ear," Proc. Natl. Acad. Sci. U.S.A. **109**(24), 9529–9534 (2012).

16. G. L. Monroy, R. L. Shelton, R. M. Nolan, C. T. Nguyen, M. A. Novak, M. C. Hill, D. T. McCormick, and S. A. Boppart, "Noninvasive depth-resolved optical measurements of the tympanic membrane and middle ear for differentiating otitis media," The Laryngoscope **125**(8), E276–E282 (2015).

17. S. Van der Jeught, J. J. Dirckx, J. R. Aerts, A. Bradu, A. G. Podoleanu, and J. A. Buytaert, "Full-field thickness distribution of human tympanic membrane obtained with optical coherence tomography," J. Assoc. Res. Otolaryngol. **14**(4), 483–494 (2013).

18. K. Uebo, A. Kodama, Y. Oka, and T. Ishii, "Thickness of normal human tympanic membrane," Ear Research Japan **19**(1), 70–73 (1988).

19. C. B. Ruah, P. A. Schachern, D. Zelterman, M. M. Paparella, and T. H. Yoon, "Age-related morphologic changes in the human tympanic membrane: a light and electron microscopic study," Arch. Otolaryngol. Head Neck Surg. **117**(6), 627–634 (1991).

20. L. C. Kuypers, W. F. Decraemer, and J. J. Dirckx, "Thickness distribution of fresh and preserved human eardrums measured with confocal microscopy," Otology & Neurotology **27**(2), 256–264 (2006).

21. G. Hüttmann, P. Koch, and R. Birngruber, "Linear OCT," in *Optical Coherence Tomography*, W. Drexler, J. G. Fujimoto ed. (Springer, 2008).

22. R. L. Shelton, W. Jung, S. I. Sayegh, D. T. McCormick, J. Kim, and S. A. Boppart, "Optical coherence tomography for advanced screening in the primary care office," J. Biophotonics **7**(7), 525–533 (2014).

23. J. Ren, J. Wu, E. J. McDowell, and C. Yang, "Manual-scanning optical coherence tomography probe based on position tracking," Opt. Lett. **34**(21), 3400–3402 (2009).

24. B. Y. Yeo, R. A. McLaughlin, R. W. Kirk, and D. D. Sampson, "Enabling freehand lateral scanning of optical coherence tomography needle probes with a magnetic tracking system," Biomed. Opt. Express **3**(7), 1565–1578 (2012).

25. N. Iftimia, G. Maguluri, E. W. Chang, S. Chang, J. Magill, and W. Brugge, "Hand scanning optical coherence tomography imaging using encoder feedback," Opt. Lett. **39**(24), 6807–6810 (2014).

26. P. Pande, G. L. Monroy, R. M. Nolan, R. L. Shelton, and S. A. Boppart, "Sensor-based technique for manually scanned hand-held optical coherence tomography imaging," J. Sensors **501**, 8154809 (2016).

27. A. Ahmad, S. G. Adie, E. J. Chaney, U. Sharma, and S. A. Boppart, "Cross-correlation-based image acquisition technique for manually-scanned optical coherence tomography," Opt. Express **17**(10), 8125–8136 (2009).

28. X. Liu, Y. Huang, and J. U. Kang, "Distortion-free freehand-scanning OCT implemented with real-time scanning speed variance correction," Opt. Express **20**(15), 16567–16583 (2012).

29. D. Stifter, "Beyond biomedicine: a review of alternative applications and developments for optical coherence tomography," Appl. Phys. B **88**(3), 337–357 (2007).

30. C. Li, J. A. Zeitler, Y. Dong, and Y.-C. Shen, "Non-destructive evaluation of polymer coating structures on pharmaceutical pellets using full-field optical coherence tomography," J. of Pharm. Sci. **103**(1), 161–166 (2014).

1. Introduction

A typical Optical Coherence Tomography (OCT) system consists of an arrangement similar to the Michaelson interferometer, where light from a low coherence source is split into reference and sample arms. The light beam in the reference arm is directed back after reflection from a mirror and is made to combine with the backscattered light from the sample to obtain an interference signal, which contains information about the depth reflectivity profile of the sample, which is called an A-line. OCT is most commonly performed in either the time- or frequency-domain [1]. In time-domain OCT (TD-OCT), the mirror in the reference arm is mechanically translated through the full imaging depth range, typically by using a rapid scanning optical delay line (RSOD) in the reference arm. At each position of the reference mirror, the intensity of the interference signal is recorded by a photodetector and the depth reflectivity profile is obtained by analyzing the envelope of the temporal interference pattern recorded by the photodetector [2]. Due to the presence of a mechanically driven reference mirror, TD-OCT systems are less stable and have limited data acquisition speed compared to frequency-domain OCT (FD-OCT) systems.

FD-OCT differs from TD-OCT in that the mirror in the reference arm of a FD-OCT system is fixed and the spectrally resolved inteferogram is recorded by using a spectrometer and a line-scan camera. The depth-resolved reflectivity profile, in a FD-OCT system is obtained by performing a Fourier transform of the interference signal recorded by the detector [3]. In comparison with TD-OCT systems, FD-OCT systems have better stability, significantly faster imaging capability, and higher signal-to-noise (SNR) [4]. The superior performance of FD-OCT systems, however, come at a price of an increase in complexity in system design and data-processing. Moreover, compared to TD-OCT, FD-OCT systems are significantly more expensive to build due to components such as a high-resolution spectrometer and line-scan camera.

Since OCT was first demonstrated in the early 1990s, the technology has matured over the years and has progressed from being a research tool that was limited mostly to academic labs to being a commercial instrument used in specialized clinical settings. While on one hand, persistent efforts are being made to further push the limits of OCT technology by developing faster and more sophisticated technologies, such as the recent research thrust in the development of faster swept-source based systems, on the other hand, considerable effort is also being put in developing affordable and compact imaging probes based on existing OCT technologies [5–9]. In this article, we report the development of a low-cost hand-held low-coherence interferometric imaging system, which is based on the principle of linear optical coherence tomography (L-OCT), a technique which was proposed in the early 2000s as a simpler alternative to the conventional TD- and FD-OCT [10–12]. Unlike traditional Michaelson interferometric setups, in L-OCT, the reference and sample beams are made to combine on the detector at an angle α. As a result, the depth dependent reflectivity information of the sample gets encoded as a spatially varying intensity of the interference pattern recorded by the detector, which is subsequently analyzed to obtain the A-line. In the original design of L-OCT and its several variants proposed subsequently, a line-scan camera was used as the detector. In our design, we propose the use of a 2-D CMOS camera as the detector instead of a line-scan camera, which allows for a less expensive and simpler optical design. The rest of the article is structured as follows. We first present a bench-top implementation and validation of the proposed L-OCT system. Next, the design of a contact-based hand-held imaging probe is presented along with a comparison of its imaging performance with a research-grade state-of-the-art Fourier-domain low coherence interferometry (LCI) system by imaging several biological and non-biological samples. Finally, we present the prototype of a hand-held imaging probe designed specifically for tympanic membrane (TM) imaging. We end with a discussion of the proposed technique and possible future work.

2. Methods and results

The schematic of our bench-top L-OCT system is shown in Fig 1(a). As in the traditional Michaelson interferometer, light from a broadband superluminescent diode (SLD) (Superlum, D-840-HP, $\lambda_0 = 840$ nm, $\Delta\lambda = 100$ nm) is split into sample and reference beams. A tilt is introduced in the reference beam through steering optics before it is combined with the back-scattered light from the sample to illuminate a 4096×2160 CMOS array (Point Grey, Flea3 8.8 MP Color USB3 Vision, 21 fps). To align the two beams, the sample path was first set up and the camera position was determined by aligning the sample beam using mirror as a sample. Once the camera position was determined, the sample beam was blocked and the reference beam was coarsely centered on the detector by adjusting the kinematic mounts holding the mirrors in the reference arm. Subsequently, the sample beam was unblocked and the fine adjustment of the reference beam was performed simultaneously with the adjustment of the path length in the reference arm to match the sample arm's path length. The choice of the camera was primarily motivated by its reasonable pixel pitch of 1.55 μm and the sufficiently large number of pixels (4096 pixels) along the direction that encodes the depth information. These parameters play an important role in determining the performance of the imaging system, as discussed later in the

article. The resulting spatial fringe pattern obtained on the CMOS detector encodes information about the relative time-of-flight of photons between the sample and reference arms, which is subsequently digitally processed to obtain depth-resolved reflectivity profiles from the sample.

The data processing flow for our L-OCT system is shown in Fig. 1(b) for the case when a mirror is used as the sample. To better understand the processing steps involved, it is worthwhile to note that the interference pattern along one spatial dimension (assumed to be x without loss of generality) recorded by the detector $I(x)$ can be expressed in terms of system parameters as:

$$I(x) = I_S(x) + I_R(x) + 2\sqrt{I_S I_R} \sin\left(\frac{2\pi\alpha x}{\lambda}\right)\gamma(x) \tag{1}$$

where I_S and I_R represent the sample and reference intensities, α denotes the angle between the sample and reference beams and $\gamma(x)$ denotes the spatial coherence function, which is related to the power spectral dependence of the light source by a Fourier transform. As is evident from the above expression, the spatial carrier frequency of the interference pattern modulated by the coherence function of the source is a function of the angle α enclosed by the sample and reference beams. Also, different depths of the sample cause modulation in the interference pattern at different spatial coordinates. The upper left panel in Fig.1(b) shows the 2-D spatial interference pattern obtained by imaging a single reflector (mirror) as the sample. As expected based on the aforementioned discussion of L-OCT, the interference pattern shows a single band of fringes (at the center of the "raw image"); the width of the band determined by the width of the coherence function of the source. To extract the A-line from the raw image, a 2-D Fourier transform demodulation is performed [13], which involves taking the 2-D Fourier transform of the raw image followed by band pass filtering in the frequency domain and finally taking the inverse Fourier transform to obtain the demodulated image shown in the top right and bottom right panels in Fig. 1(b). The demodulated image contains along its rows, the A-line, which in the case of a mirror as the sample, is just the coherence function or the point spread function (PSF) of the system. The other spatial dimension (vertical columns in the demodulated image) contains repetitions of the same A-line, which is averaged to enhance the SNR of the resultant A-line shown in the bottom left panel of Fig. 1(b). The axial resolution and the SNR of our bench-top system was measured to be approximately 5.2 μm and 80 dB, respectively. Sensitivity roll-off of the system was estimated to be 3.7 dB over a depth of 0.15 mm.

After characterizing the axial resolution and SNR of the bench-top system, we validated the imaging performance by obtaining B-scans of various standard samples used in OCT imaging by translating the sample along the lateral dimension using a motorized translation stage in increments of 10 μm, while recording the A-lines for each position of the sample. Figure 2(a) shows the B-scan obtained from a scotch tape roll, where different layers of the tape roll can be seen as alternating bright and dark bands. Fig. 2(b) shows the B-scan obtained by imaging a grape. As expected, the juice vacuoles show up as hexagonal patterns in the B-scan. Finally, we imaged an apple to visualize the various microstructures present therein. The layer of wax can be seen as the bright top surface in the B-scan shown in Fig. 2(c), followed by a dark and bright band, which correspond to the cuticle and epidermis layers (labeled Cu and Ep in Fig. 2(c)), where the bright structures correspond to the cell walls.

After validating our bench-top L-OCT system, we designed a hand-held probe for contact-based imaging. Figure 3(a) and (b) shows the Solidworks rendering and the actual prototype of the imaging probe, respectively. The physical dimensions of this probe was approximately 20 cm × 10 cm × 4 cm and its weight was 521 g. To assess the performance of our hand-held device, we compared the A-lines obtained from various samples by using our probe with those obtained by using a state-of-the-art Fourier-domain LCI system reported in [14]. The results of the comparison are presented in Fig. 4. Three samples, namely, a double-sided tape roll, a pharmaceutical tablet, and finger skin were imaged using the proposed L-OCT hand-held probe
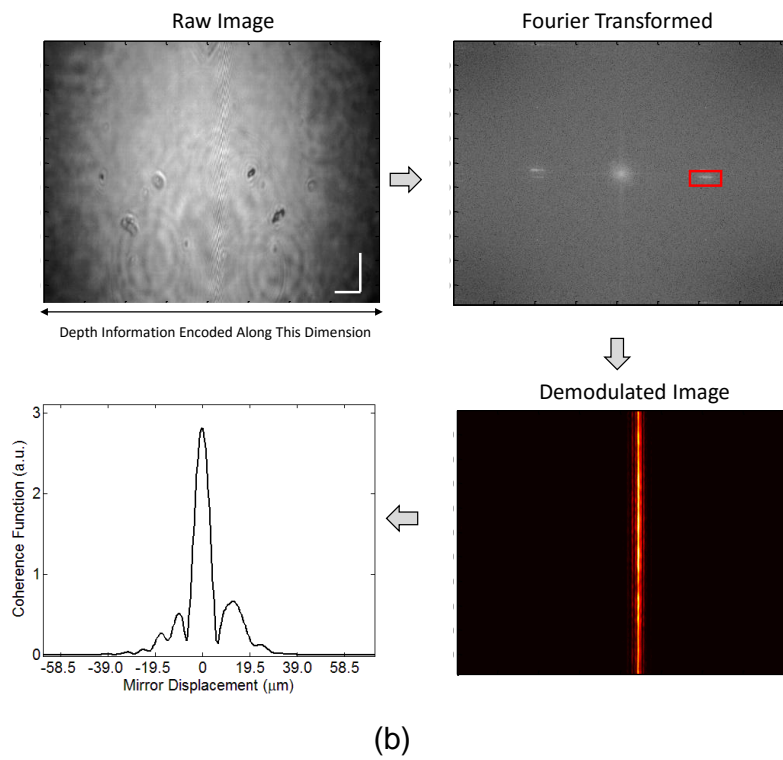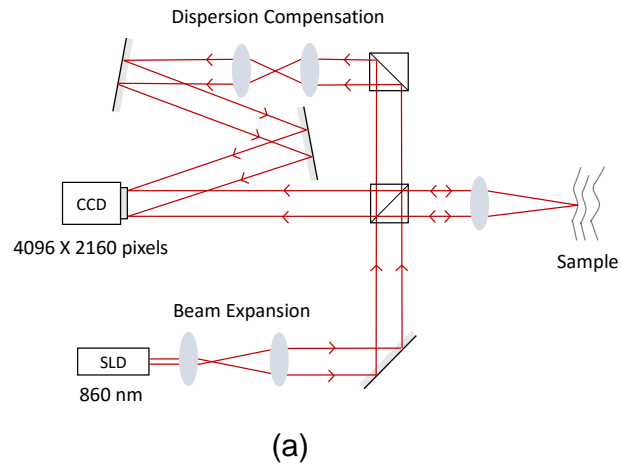
(a)

(b)

Fig. 1. (a) Schematic of the bench-top implementation of the proposed L-OCT system. (b) Data processing flow illustrating the sequence of steps to extract an A-line from the fringe pattern captured by the detector. Scale bars represent 0.5 mm.
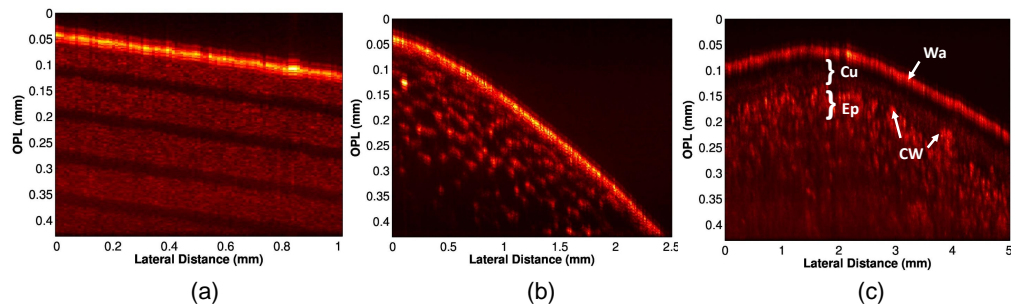
Fig. 2. Representative B-scans obtained by laterally translating the samples. (a) Scotch tape roll. (b) Grape. (c) Apple. (Wa: Wax, Cu: Cuticle, Ep: Epidermis, CW: Cell Wall).
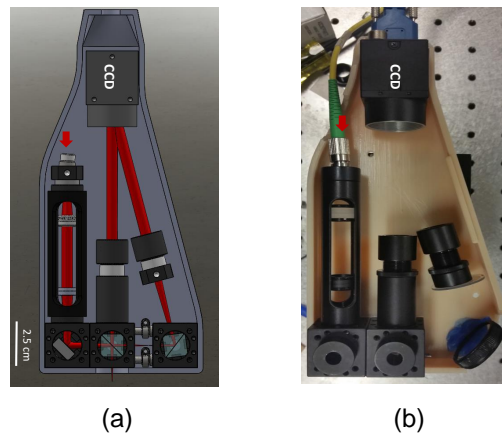

Fig. 3. (a) Solidworks rendering of a prototype of the contact-based imaging probe. (b) Actual probe.

(left column in Fig. 4) and a Fourier-domain LCI system (right column in Fig. 4) for comparison. It must be noted that the A-lines shown in Fig. 4 do not correspond to the exact same spot on the sample because the sample had to be physically moved between the two systems for imaging. However, care was taken to ensure that the imaging sites were in the same general area. As can be seen, generally, when comparing the gross structural features, the two systems perform comparably. The A-lines obtained from the double-sided tape has several peaks corresponding to the different layers in the tape roll. In the case of the pharmaceutical tablet, the coating on the tablet appears as a strong peak in the A-lines. Finally, for finger skin, the air-epidermis and the epidermis-dermis junctions can be easily identified as two prominent peaks in the A-lines.

Motivated by the successful imaging performance of our bench-top and contact imaging probe, we designed a hand-held probe for depth-ranging and imaging of the tympanic membrane (TM). TM thickness measurements and imaging are particularly attractive applications of the proposed L-OCT system, since the A-line measurements of the TM, where the two surfaces of the TM, namely the epidermal (outside surface) and mucosal (inside surface) appear as two distinct peaks, can provide thickness estimates of the TM. TM thickness has a strong association with the state and functioning of the middle-ear and is known to provide diagnostically useful information about several middle-ear pathologies. For example, our group has in the past shown that the thickness of the TM in healthy human subjects is significantly different from that in subjects
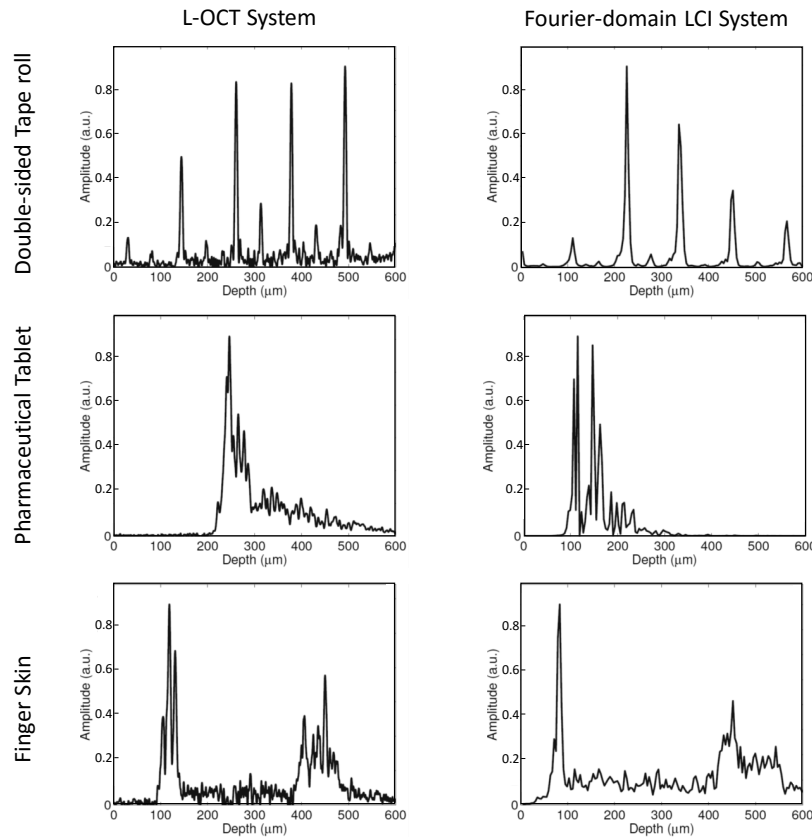
Fig. 4. Imaging performance of the proposed system. The left column shows the A-lines obtained from imaging different samples (along rows) obtained from the proposed system, compared with A-lines obtained from imaging the same samples with a state-of-the-art Fourier-domain LCI system (right column).

with acute and chronic otitis media (OM) [15, 16]. The schematic and the actual imaging probe are shown in Fig. 5. The design consists of two modules for L-OCT imaging and video otoscopic imaging, respectively. The L-OCT module design is similar to the basic L-OCT design used in our bench-top and contact probe designs. For adjusting the optical path length of the reference arm of the L-OCT system, a small form factor translation stage (Thorlabs, DT12) was included in the probe. The two beam paths for OCT and video imaging were separated using a dichroic mirror (labeled DM in the schematic). The video otoscopic imaging is critical for ear imaging to aim the imaging beam at the right location on the TM. The probe nose-cone, which integrates a fiber bundle arranged concentrically around the tip, was obtained from a commercial otoscope (R.A. Bach Diagnostics). White light for video imaging of the TM was delivered by illuminating the distal end of the fiber bundle using an LED. The TM surface was imaged onto a miniature USB camera (Ximea, MU9PC-MH) using appropriate focusing optics. The data acquired from the proposed L-OCT probe comprises a surface image of the sample and corresponding A-line acquired from a point on the sample, as shown in the insets in Fig. 5 for the case of imaging a sheet of paper (the inset next to the camera for surface imaging, C_2, shows the surface image, whereas the inset next to the CMOS detector for L-OCT, C_1, shows the corresponding A-line). The physical dimensions of our hand-held probe was 25.4 cm × 16.5 cm × 5.1 cm and it weighs
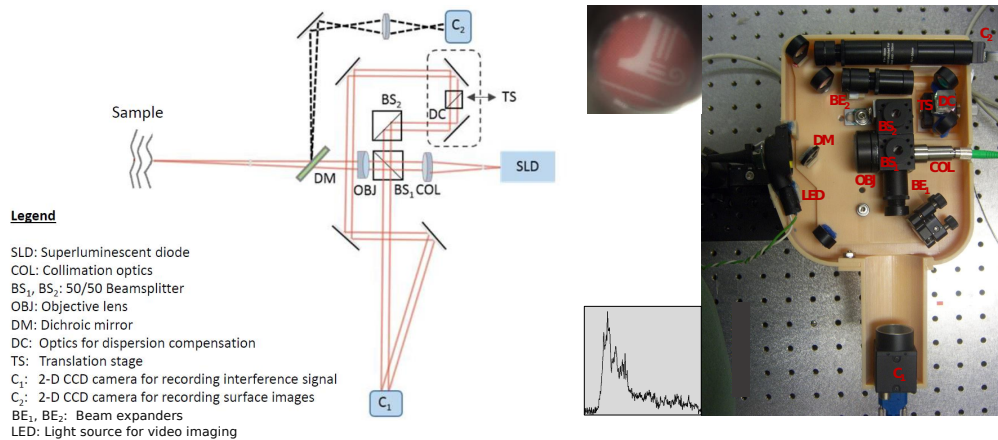
Fig. 5. Schematic of the hand-held imaging probe for *in vivo* ear imaging and a photograph of the actual probe. The insets show the surface image of the sheet of paper used as the sample (top left) and the corresponding A-line acquired from a point on the sample (bottom left).

707.6 g.

As in the case of the bench-top system and contact-based probe, we validated our TM imaging probe by imaging several samples, which included a coverslip, a double-sided tape roll, and a plastic TM phantom. The A-lines for these are shown in Fig. 6(a)-(c). Unlike the benchtop implementation, where the dispersion was accurately matched by using a pair of lenses in the reference arm that were identical to the objective lens in the sample arm, in the hand-held probe, the dispersion was mitigated by simply adding extra glass in the reference arm (labeled DC in Fig. 5), which was not adequate to fully match the dispersion characteristics of the objective and the dichroic present in the sample arm. The imperfect dispersion compensation in the hand-held probe resulting from the unmatched dispersion in the two arms of the hand-held probe was responsible for the asymmetric profile of the PSF, which is evident in images shown in Fig. 6. The effect of dispersion mismatch could be reduced by using computational methods for dispersion compensation.. Finally, we imaged the TM of a healthy volunteer. Inset in Fig. 6(d) shows the surface image of the TM and the A-line obtained from a point on the TM, marked by a red asterisk in the inset. The thickness of the TM (assuming a refractive index of 1.4 for the TM [17]) was estimated to be 106 μm, which lies in the range of thickness values expected for a healthy TM [17–20].

3. Discussion

Since the proposed imaging system is based on the principle of L-OCT, it shares the limitations of L-OCT, which can be better understood by noting an important aspect of L-OCT, which is that to meet the Nyquist criterion, the pixel frequency of the detector needs to be at least twice the frequency of the fringe pattern (argument of the sine term in Eq. (1)). Moreover, since the depth information is mapped on to the spatial dimension of the detector, the imaging depth is proportional to the number of pixels on the detector. This means that for a given sensor, a larger imaging range can be achieved by increasing the angle enclosed by the reference and sample beams only to an extent permitted by the Nyquist criterion. The interplay between different system parameters is also evident from the expression for maximum achievable SNR of a L-OCT system. As discussed in [21], the SNR of a L-OCT can be expressed in terms of the system
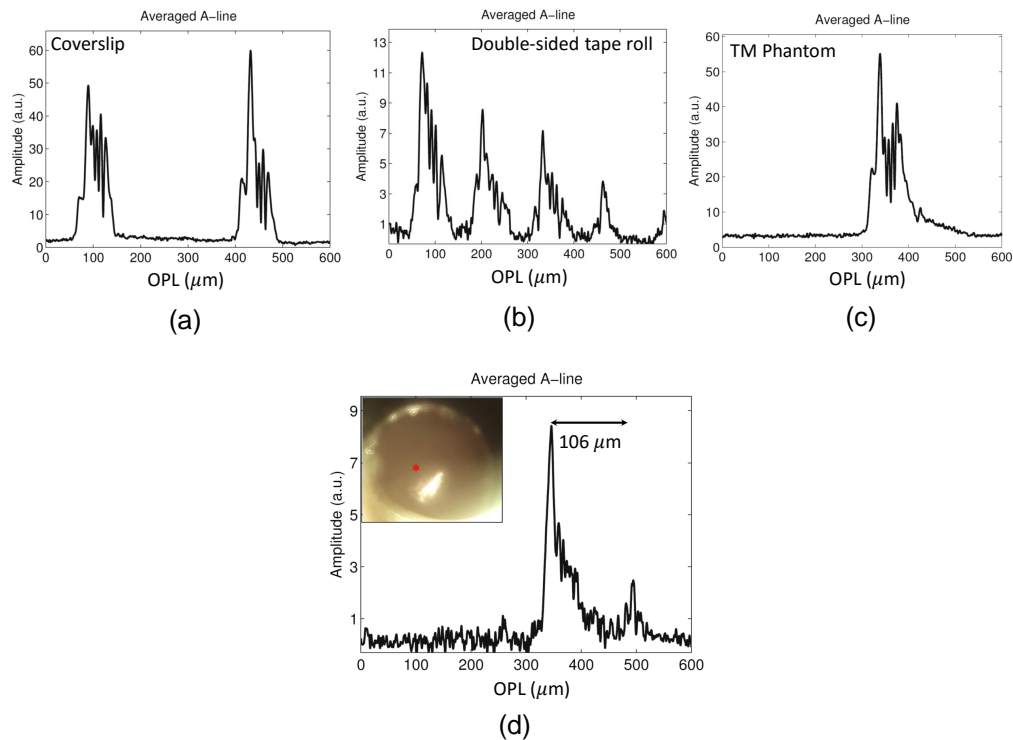
Fig. 6. A-lines obtained by using the probe for TM imaging from various samples. (a) Stack of coverslips (b) Double-sided tape roll (c) Plastic sheet used as TM phantom (d) *In vivo* human TM.

parameters as follows:

$$\text{SNR} \propto \frac{\text{FWC}}{z_{max}} \qquad (2)$$

where FWC denotes the full well capacity of the sensor and z_{max} represents the imaging depth. From the above expression, it follows that for a fixed imaging range, increasing the SNR requires an increase in the FWC of the sensor pixels. This in turn means increasing the pixel pitch of the detector, which would entail reducing the angle between the sample and reference beams to avoid aliasing and simultaneously using a detector with larger number of pixels to maintain the imaging range. These are some of the important considerations that need to be taken into account while designing an L-OCT system.

The total cost of all the components used in our hand-held probe, excluding the source, was $3900. The standard off-the-shelf optical components cost approximately $2100, the detector was priced at $1100, and the camera for video imaging costs $700. Unsurprisingly, this is significantly lower than the cost of a FD-OCT system. For instance, the cost of just the detector module comprising the spectrometer and line-scan camera in the FD-LCI system developed in our lab and used to acquire the data presented in Fig. 4 was around $14,000. For a traditional L-OCT system that uses a line-scan camera, the major difference in cost compared to our system would come from the use of a line-scan camera, instead of a 2-D sensor, which can cost around $4500. More importantly, the use of cylindrical optics to focus the beam on a line-scan camera makes the system design more complicated than the design of the proposed technique. For a TD-OCT system, the major contribution to the overall system cost comes from the fast photo-

detector, which can be as expensive as $1500, and rapid scanning optical delay line, cost of which can vary between $3500 - $5000, depending on the mechanism, range, speed etc. Thus, while a simple, albeit more difficult to set-up mechanism that involves mounting a mirror on a precision translation stage would be cheaper, the cost of a more sophisticated and easier-to-use integrated delay line would fall on the higher end of the price range. To summarize the cost comparison, the main difference in cost between our system and other OCT systems come from the use of different detectors (spectrometer module in FD-OCT *vs.* line-scan camera in a standard implementation of L-OCT *vs.* photo-detector and optical delay line in TD-OCT *vs.* 2-D camera in our design) and the optics (standard off-the-shelf and low-cost components *vs.* expensive and/or nonstandard parts). The cost of the source, which in the case of an SLD is a few thousands of dollars, contributes equally to the overall cost of the different OCT systems compared above. An exception to this is a swept-source system, where the source is perhaps the most expensive component and can cost tens of thousands of dollars.

One of the main challenges of imaging using our current probe was to ensure the stability of the interferometric setup during data acquisition, which was caused by the small amount of unavoidable buckling of the probe enclosure that resulted from the use of polymer material used for 3-D printing. This challenge could have been potentially overcome by using a machine fabricated metal housing for the probe. Moreover, the slow frame rate of 21 fps of the camera used as the detector prevented us from averaging over several A-lines, which could have improved the signal quality significantly. With the recent advances in 2-D CMOS technology and reduction in sensor costs, we believe that overcoming this limitation would not be extremely difficult. Finally, the form-factor of our probe (25.4 cm × 16.5 cm × 5.1 cm) was somewhat larger than what would be ideally desired for a hand-held device. Several hand-held probes having widely varying dimensions have been reported in the literature. For example, an earlier version of a FD-OCT probe developed by our group measured 11.5 cm × 11.5 cm × 6.3 cm [5]. A SS-OCT based probe for eye imaging reported in [6] has dimensions of 15.1 cm × 18.2 cm × 7.4 cm. Likewise, another SS-OCT probe for intraoperative eye imaging measures 13.7 cm × 3.7 cm × 3.2 cm [7]. Another hand-held probe for optical coherence microscopy imaging reported in [8] had physical dimensions of 15 cm × 11.5 cm × 10 cm. However, we would like to point out that unlike these probes, ours is self-contained in that all the necessary components, except the source, are housed in the probe. Nevertheless, improving the system design to further reduce the footprint of the probe would significantly improve the maneuverability and ease-of-use of the device.

In our hand-held probe prototypes, we do not have a mechanism for lateral scanning to generate cross-sectional 2D images (B-scans). As stated earlier, the B-scans shown in Fig. 2 were generated by physically translating the sample using a motorized translation stage. The purpose of obtaining B-scans was to validate the proposed imaging system because B-scans are capable of providing better insights into the performance of an imaging system by revealing additional structural features in the sample not visible with an A-line alone, which for complex samples are less intuitive to interpret. In applications where spatial depth-resolved information is required, the proposed imaging system can be combined with several hardware and software lateral scanning approaches developed by our group and others. The simplest, albeit an expensive approach, could be the incorporation of a microelectromechanical systems (MEMS) scanner in the hand-held imaging probe [22]. Another hardware-based approach could involve a sensor-based manual scanning technique, where real-time feedback from an optical motion sensor is used to trigger data acquisition, which works by adaptively altering the trigger rate based on the instantaneous scan velocity, enabling OCT imaging over a large lateral field-of-view [23–26]. Amongst software based methods, an approach based on the decorrelation of sequentially acquired A-lines by moving the imaging probe over the sample could be used [27, 28]. Alternatively, an image-processing based approach described in [14] can be followed, wherein, video data of the sample surface is acquired simultaneously with A-lines. The frames of the video-data can then be

co-registered using image processing techniques to obtain information about the relative spatial locations of the points at which A-line data is acquired, which can be used to assemble B-scans from A-lines. However, to enable B-scan acquisition using the existing imaging probe, in conjunction with any of the aforementioned methods, would require a faster detector. In its current form, we envision the use of the proposed technique primarily as a LCI device, which could still be useful for several applications, such as the one presented in an earlier work published by our group [15], where it was shown that LCI-based tympanic membrane thickness measurements were capable of providing diagnostically useful information.

In summary, we reported the development of a low-cost hand-held optical coherence ranging and imaging system based on the principle of L-OCT. The imaging performance of the proposed system was compared with a standard Fourier-domain low coherence interferometry system by imaging several biological and non-biological samples. The advantage of our technique is that it is simple to implement and requires only standard off-the-shelf inexpensive optical components. This, however, comes at the cost of reduced SNR and imaging depth. We therefore believe that the proposed technique might be a suitable choice for less demanding imaging applications where the imaging depth and SNR can be traded for lower cost and simpler optical design. Two potentially useful applications, as demonstrated in this study, could be *in vivo* imaging of the human TM to determine the TM thickness, which could be used to detect the presence of any middle ear biofilm or effusion, and relatively newer applications, such as visualization of the sub-surface features of materials for non-destructive evaluation and quality inspection, where OCT has been recently used [29, 30].

Disclosures

R.L.S., R.M.N., and S.A.B. have a financial interest in PhotoniCare, Inc. PhotoniCare did not, however, sponsor this research. The remaining authors do not have any conflict of interest.